frontiers | Frontiers in Mechanical Engineering

TYPE Original Research
PUBLISHED 13 October 2023
DOI 10.3389/fmech.2023.1240761

OPEN ACCESS

EDITED BY
Tanvir I. Farouk,
University of South Carolina,
United States

REVIEWED BY
Fahd Alam,
Exponent, United States
Sheikh Ahmed,
Honeywell Aerospace, United States

*CORRESPONDENCE
S. Castellani,
simone.castellani@unifi.it

RECEIVED 15 June 2023
ACCEPTED 25 September 2023
PUBLISHED 13 October 2023

CITATION
Castellani S, Nassini PC and Andreini A (2023), Optimization of a two-step CH_4/air reaction mechanism in a CO_2-enriched environment for high-fidelity combustion simulations.
Front. Mech. Eng 9:1240761.
doi: 10.3389/fmech.2023.1240761

Optimization of a two-step CH_4/air reaction mechanism in a CO_2-enriched environment for high-fidelity combustion simulations

S. Castellani*, P. C. Nassini and A. Andreini

Department of Industrial Engineering (DIEF), University of Florence, Florence, Italy

In the gas turbine framework, the adoption of carbon capture and storage (CCS) systems coupled with strategies to improve the exhaust CO_2 content is a promising technology to abate the carbon footprint of such machines. However, any departure of the oxidant from the air can compromise the accuracy of the conventional models to represent the combustion process. In this work, the effect of the CO_2 enrichment of the mixture on an atmospheric premixed swirled flame is investigated by means of large eddy simulation (LES), comparing the numerical predictions with the experimental results. The high-fidelity numerical model features a dedicated global reaction mechanism derived through an in-house optimization procedure presented in this study. The chemical scheme is obtained by optimizing a widely used CH_4–air two-step mechanism to improve key flame parameters such as the laminar flame speed and thickness and the resistance of the flame to the stretch with moderate CO_2 dilution. The numerical results are analyzed in terms of flame shape, heat losses, and pressure fluctuations, showing a promising agreement with the experimental measurements and demonstrating the capabilities of the numerical model for CO_2-diluted combustion.

KEYWORDS

exhaust gas recirculation, artificially thickened flame model, high-fidelity simulation, reaction mechanism calibration, large eddy simulation

1 Introduction

The unprecedented high levels of greenhouse gases in the atmosphere impose the adoption of concrete solutions for containing the pollutant emissions of the energy sector. Despite the increasing share of renewable sources, conventional systems based on fossil fuel combustion, such as gas turbines, still require new clean technologies to mitigate CO_2 emissions. There are two possible ways to considerably reduce CO_2 emissions: first is to use carbon-free fuels (such as H_2) and second is to burn carbon-containing fuels by coupling gas turbines with carbon capture and storage (CCS) systems. However, the use of a CCS system can introduce a significant penalty (reduction) in the power plant's total efficiency (Li et al., 2011), so important technical efforts must be focused on the maximization of the CCS efficiency, strictly linked with the CO_2 concentration in the exhaust plumes (Li et al., 2011). The introduction of exhaust gas recirculation (EGR) in gas turbines allows the maximization of the CO_2 content in the exhaust gases, significantly increasing the efficiency of the CCS

system. Moreover, as pointed out by Burnes et al. (2020), the recirculation of a portion of the exhaust gases decreases the exhaust mass flow for a fixed power output, thus allowing a reduction in the needed CCS system's size. These aspects make any increase in the portion of recirculating gases convenient for the overall system efficiency, enabling EGR as a very promising combustion strategy when combined with CCS.

On the other hand, there are several limiting aspects when the EGR level is increased; first, upon increasing EGR, the mixture gets depleted of O_2, and according to this, the theoretical maximum EGR level ensures complete O_2 consumption in the exhaust gases (Li et al., 2011; Burnes et al., 2020). This limit is only theoretical as, in practical combustor operations, emissions and flame stability limits are reached earlier. From the emissions point of view, EGR is found to be beneficial for NOx reduction under gas turbine conditions owing to several different contributions (Hejie et al., 2009). However, CO emissions can be negatively affected by EGR, and the containment of these emissions can be a potential limit to the increase in the EGR level (Burdet et al., 2010; Guethe et al., 2011).

As mentioned previously, in the case of beforehand emissions, the increase in the CO_2 content of the fresh mixture strongly affects the reactivity by modifying the stability limits of the combustors. To investigate the thermodynamics and kinetics effect of such CO_2 enrichment on the flame speed, several experimental and numerical laminar flame investigations have been performed in the literature (Halter et al., 2009; Galmiche et al., 2011; Chan et al., 2015; Chen et al., 2020; Duva et al., 2020; Xie et al., 2020). Xie et al. (2020) numerically isolated different contributions that compete for such laminar flame speed (LFS) reduction, showing that CO_2 is far from being inert from the kinetics perspective. Because of this expected change in the mixture characteristics, to ensure wide combustor operability margins with high EGR levels, modifications in the combustor architecture would be necessary, and the numerical modeling will provide valuable contributions to support such efforts. The effectiveness of the existing numerical models must be validated against experimental measurements for use as a reliable design tool.

Several experimental studies have been conducted in the past years to investigate the effect of CO_2 addition on the flame stability and emissions of actual combustor systems. Evulet et al. (2009) successfully operated the 9FB DLN burner up to 35% of the EGR level without any major design modifications, measuring a CO_2 volume concentration of 8% in the plumes. They concluded that the admitted EGR level could be further extended with the addition of a small pilot percentage, which would enhance flame stabilization without affecting NOx emissions. The concept of staged combustion uses a completely different machine architecture but with the same effects from the plume composition's perspective. This technology has been found very effective as well managing high EGR levels while maintaining the stability margin at the same time. Burdet et al. (2010) experimentally operated the DLN SEV single-cup burner under gas turbine-relevant conditions with very low residual O_2 in the exhaust gases (2%–5% by volume). Apart from the studies carried out on industrial burners, the effect of CO_2 addition on the flame has also been widely investigated in simplified laboratory burners (Kobayashi et al., 2007; Cohé et al., 2009; Erete et al., 2017; Han et al., 2017; Han et al., 2018). Nevertheless, in the literature, few experimental studies can be found on swirled stabilized flames (De Persis et al., 2013; Jourdaine et al., 2017; Vandel et al., 2020). To the best of the authors' knowledge, the experimental study carried out by De Persis et al. (2013) is the only one that experimentally investigates a CO_2-enriched methane–air swirl stabilized flame. In this work, several conditions have been studied to investigate the effect of CO_2 enrichment on flame stabilization. Trying to numerically reproduce some of these experimental test points, high-fidelity numerical simulations have been performed to assess the model prediction capacity and investigate the predicted flame characteristics with and without CO_2 addition. In a generalized context, the numerical model must be adequate to characterize the combustor behavior near the blow-out limit because it would be very useful to investigate the blow-out mechanism to extend the stability margin of the combustor. The correct prediction of these conditions depends on the ability of the numerical model to correctly reproduce complex behaviors, such as heat loss and stretch effect on the flame front (Nassini et al., 2021).

In this work, the artificially thickened flame model (ATFM) is used for the description of the turbulence chemistry interaction. In this model, the accuracy in the prediction of the stretch and heat loss effects is largely entrusted to the chosen chemical mechanism. In the literature, different approaches can be found to characterize the chemistry. Franzelli (2011)compared different chemical reaction mechanisms to identify the best cost–accuracy compromise. From this perspective, the two-step chemistry is very cost-effective, and this peculiarity motivates the choice of such chemical reaction mechanisms for this study. More recently, Cailler et al. (2020) presented a work on an advanced optimization method for one- and two-step chemistry. They completely redefined the concept of species, considering virtual species optimized for the specific conditions of interest. In this study, the CH_4–air BFER* (Franzelli, 2011) reaction mechanism has been taken as a reference reaction mechanism. However, the LFS prediction of this mechanism worsens rapidly outside the operating conditions for which it has been developed and optimized. Therefore, the addition of a non-negligible amount of CO_2 to the fresh mixture requires the mechanism to be re-optimized. Moreover, any further change in the mixture composition in terms of CO_2 content would require a mechanism readjustment, raising the need to define an automatic procedure to accomplish that task.

In Section 2, the details of the optimization of the chemical kinetics scheme are presented with a description of the automatic procedure adopted. In Section 3, the derived mechanism is applied for the investigation of a turbulent combustion test case. Regarding the test case, the description followed by the results of two high-fidelity simulations are provided, comparing the predictions with experimental data.

2 Chemical kinetics

2.1 Reaction mechanism optimization

The optimization procedure adopted has been developed in Python with a modified version of the Cantera library. This modification is necessary to ensure consistency between how the

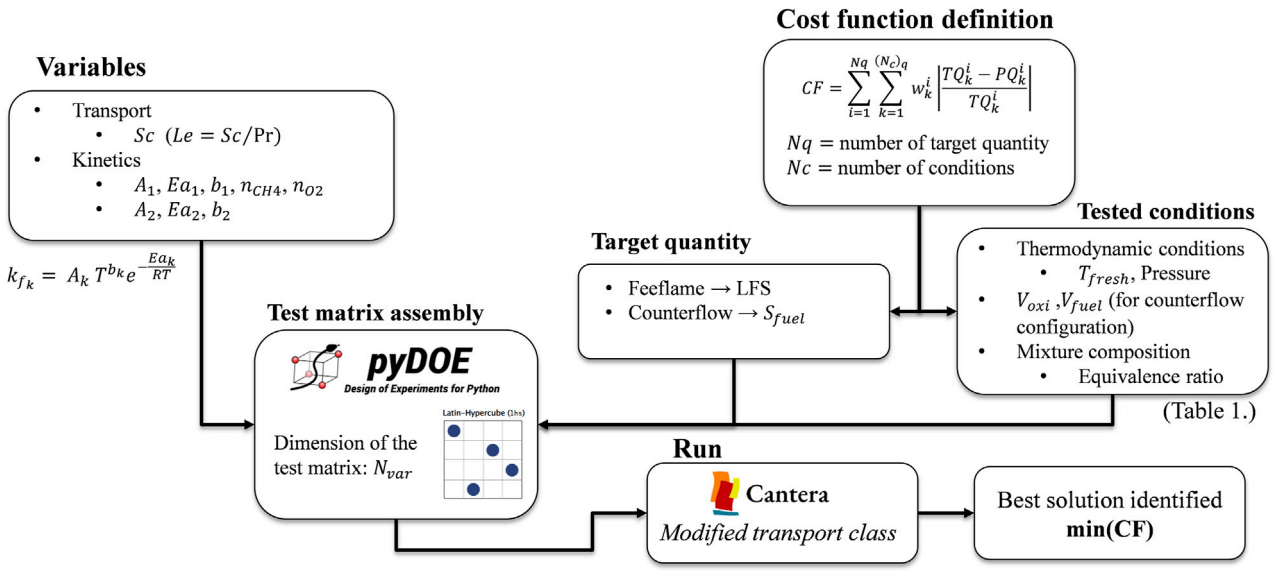

FIGURE 1
Schematic description of the reaction mechanism optimization procedure implemented in Python.

species transport, and their properties have been computed in the CFD solver and within Cantera. In this customized version of Cantera (adapted version of Cantera form CERFACS, 2017), the mass and thermal diffusion coefficients are computed considering constant Schmidt and Prandtl numbers, and the power law, reported in Eq. 1, is used for the molecular viscosity.

$$\mu = \mu_0 \left(\frac{T}{T_{ref}} \right)^b, \tag{1}$$

where the constants μ_0 and T_{ref} are calculated by fitting the molecular viscosity of the mixture from the unburned to the burned side of a freely propagating laminar flame.

The automated optimization procedure used to adapt the BFER* mechanism is schematically presented in Figure 1. First, the variables that control the kinetics and species diffusion, which have to be changed to obtain the target design requirements, must be chosen. In this work, the selected variables are all the Arrhenius constants (A_k, b_k, and Ea_k, with the subscript k referring to the reaction) and the two reaction orders (n_{CH4} *and* n_{O2}) of the first reaction. Moreover, as described in Franzelli (2011), optimization has been performed to improve the laminar flame response with respect to the strain rate.

Once the variables have been defined, for a complete definition of the optimization problem, the cost function (CF) must be specified. In this work, CF is evaluated using Eq. 2, where TQ and PQ refer, respectively, to the target quantities and the predicted quantity on the laminar flame, while Nq and Nc are the numbers of different reference quantities and the number of tested operating conditions, respectively. It must be noted that the number of conditions can be different based on quantity q. Moreover, different weights w_k^i included in the CF formulation guide the choice set of variables that enhance the model prediction under the condition of major interest.

TABLE 1 Conditions considered for the evaluation of CF (Eq. 2).

	φ [-]	T (fresh) [K]	α [1/s]
Freely propagating flame	0.6–0.8	300–700	-
Counterflow premixed flame	0.6	600 K	1e+2 - 3e+4
Fuel: CH_4			
Oxidizer: X_{CO_2} = 0.089, X_{O_2} = 0.191, and X_{N_2} = 0.720			

$$CF = \sum_{i=1}^{Nq} \sum_{k=1}^{(N_c)_q} w_k^i \left| \frac{TQ_k^i - PQ_k^i}{TQ_k^i} \right|. \tag{2}$$

The reference quantities chosen in this optimization process are LFS, computed from a 1D freely propagating flame, and the flame consumption speed S_{fuel} evaluated in the counterflow premixed flame configuration using Eq. 3. All TQs have been preliminarily computed for each condition (Nc) using GRI3.0 (Smith et al., 2000) as a reference detailed reaction mechanism. This detailed mechanism, whose accuracy is well known for the description of CH_4/air combustion, has also shown optimal performance in predicting CO_2-diluted conditions (Halter et al., 2009; Galmiche et al., 2011; Chan et al., 2015; Chen et al., 2020; Duva et al., 2020; Xie et al., 2020). The considered conditions for each flame configuration are summarized in Table 1.

$$S_{fuel} = \frac{1}{\rho_f Y_f} \int_{-\infty}^{+\infty} -\dot{\omega}_f dx. \tag{3}$$

The optimization problem is now completely defined; thus, in principle, the minimization of CF can be afforded in multiple ways. In this work, because of the simplicity of the reaction mechanism and the low computational cost of each single-flame evaluation, the

TABLE 2 Summary of the optimized mechanism kinetics and transport parameters. Units: cal, K, mol, cm³, and s.

	CH_4 oxidation reaction	$CO - CO_2$ equilibrium reaction
A	6.38e+12	1.84e+11
Ea	31,532	1.2151e+4
b	0	0.58
Reaction orders	n_{CH4} = 0.95	n_{CO} = 1
	n_{O_2} = 0.81	n_{O2_2} = 0.5
Sc [-]	1.5	

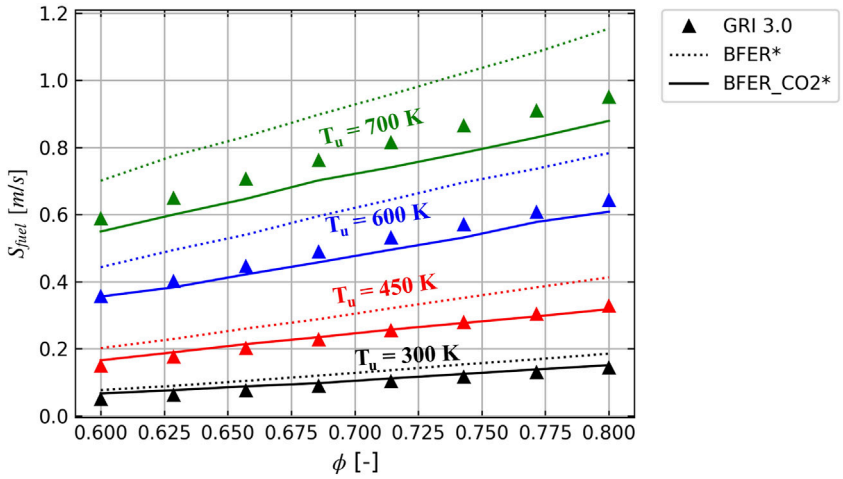

FIGURE 2
Comparison of the atmospheric unstretched LFS predicted by the original (BFER*) and the improved mechanisms (BFER_CO_2*) against the reference detailed scheme (GRI30). The colors represent the different unburnt mixture temperatures: 700 K— green, 600 K— blue, 450 K— red, and 300 K— black.

design of the experiment procedure has been chosen to explore the variable space and find the CF minima. The Latin hypercube sampling (lhs) method has been adopted to assemble the variable test matrix that has the dimension $N_{var} \times N_{samp}$. This lhs criterion allows identifying the convenient set of variables spacing over the whole design space (variable space), the boundaries of this space, and the number of sampling points N_{samp} that must be chosen. After the test matrix assembly, for each set of variables, the value of CF will be evaluated by solving a series of flames under all the conditions. It is worth noting that this process is very easily parallelizable, allowing a significant reduction in the computational cost if needed.

2.2 Chemical kinetics results

The set of variables for the new reaction mechanism, identified after the optimization process, is presented in Table 2.

The performances of the two-step BFER_CO_2* reaction mechanism in terms of LFS prediction are shown in Figure 2. This is in accordance with the reference GRI3.0 mechanism in the whole range of conditions included in the optimization. Focusing on the prediction of BFER_CO_2*, the accuracy gets better at 600 K and $\varphi = 0.6$, which are exactly the fresh mixture conditions for turbulent combustion investigations presented in the next paragraph. This was made possible by the proper choice of the w_k^i in Eq. 2. As mentioned previously, in the next turbulent combustion analysis, a perfectly premixed mixture at a well-specified temperature level will be considered. Despite that, the kinetics scheme is required to perform better in a wider range of conditions. The good LFS prediction at various unburnt temperatures shown in Figure 2 ensures the capacity of the mechanism to correctly characterize the wall heat loss impact on the flame.

The prediction of the BFER* mechanism always overestimates the reactivity, and this is expected mostly to be due to the kinetic effect of the CO_2 dissociation reactions. The BFER* was optimized for conditions in which these dissociation reactions play a marginal role, but as pointed out by Xie et al. (2020), these reactions should gain importance by increasing CO_2 enrichment, affecting the global fuel consumption capacity.

However, unlike BFER*, BFER_CO_2* does not include any pre-exponential adjustment (PEA). The PEA allows the pre-exponential factor A to be dependent on the local φ, allowing a better flame speed prediction in a wide range of φ. As a result, the validity range of the BFER_CO_2* mechanism is only within lean conditions, which are

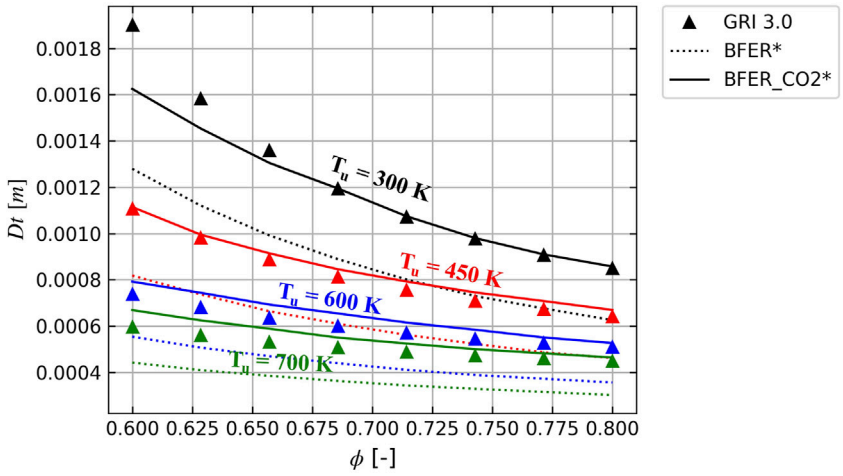

FIGURE 3
Comparison of the atmospheric unstretched laminar flame thickness predicted by the original (BFER*) and the improved mechanisms (BFER_CO_2*) against the reference detailed scheme (GRI30). The colors represent the different unburnt mixture temperatures: 700 K— green, 600 K— blue, 450 K— red, and 300 K— black.

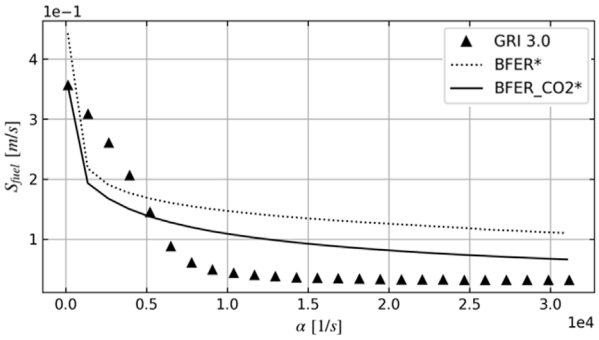

FIGURE 4
Sensitivity of LFS to the strain predicted by the original (BFER*) and improved mechanisms (BFER_CO_2*) against the reference detailed scheme (GRI30). The simulations are relative to a fresh-to-burnt counterflow premixed flame at atmospheric pressure.

the conditions of interest in this study. According to the fact that the BFER* mechanism overestimates the reactivity, it can be observed in Figure 3 that this mechanism underestimates the flame thermal thickness (Eq. 4). On the other hand, the BFER_CO_2* prediction of D_t is very close to the prediction of GRI3.0.

$$D_t = \frac{T_b - T_f}{\max\left(\left|\frac{\partial T}{\partial x}\right|\right)}. \tag{4}$$

As highlighted in Table 1, the reaction mechanism has been optimized considering counterflow premixed flames in the fresh-to-burnt configuration at various strain rate levels. The prediction of the BFER_CO_2* mechanism is not accurate in increasing the strain rate level, even though the Schmidt number has been included in the variables for optimization. In any case, the Schmidt number finally chosen allows the best reconstruction of the laminar consumption speed increasing the strain (Figure 4).

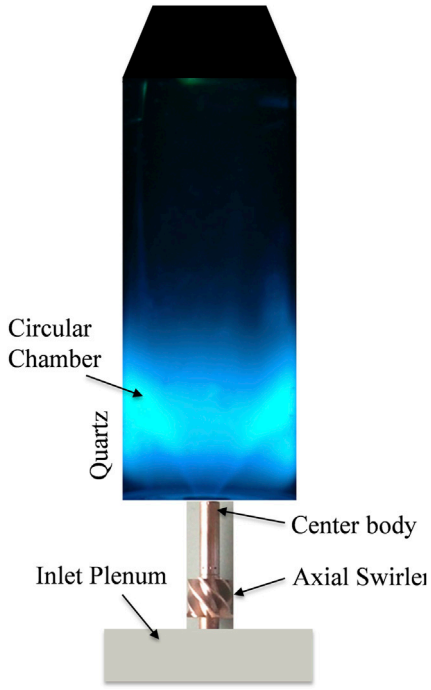

FIGURE 5
Schematic representation of the experimental facility (De Persis et al., 2013).

3 Turbulent combustion test case

An experimental test case has been chosen to assess the prediction of the kinetics scheme in the context of turbulent combustion. In the following section, the experimental facility and the selected test points are described. Afterward, the setup description and the results discussion of the high-fidelity numerical simulations are presented.

TABLE 3 Selected test point operating conditions and the corresponding unstretched laminar flame characteristics.

	0% v CO_2	8.9% v CO_2
φ	0.6	0.6
T	600 K	600 K
$\dot{m}_{tot}$	4.14 g/s	4.74 g/s
X_{CO2} (in the oxidizer)	0	0.089
D_t	0.62 mm	0.78 mm
S_{fuel}	0.46 m/s	0.35 m/s

3.1 Experimental test rig

The experimental rig is described in De Persis et al. (2013). The facility architecture, shown in Figure 5, consists of an inlet plenum, an axial swirler, and a cylindrical Herasil quartz combustion chamber. The rig is operated at atmospheric pressure under fully premixed conditions. The CO_2/air/CH_4 mixture is prepared in the mixing volume upstream the swirler so that when it enters the combustion chambers, it can reasonably be assumed perfectly premixed. The fresh mixture can be heated up to 700 K to reproduce the gas turbine combustors' inlet temperature levels. The objective of the experimental study was to investigate the effect of the CO_2 dilution on the flame stability and the corresponding change in the flame topology. The researchers have analyzed a wide range of operating conditions by varying the equivalence ratio and the CO_2 content in the fresh mixture. The observed flame shape changed from a lifted anchored condition toward the extinction, increasing the CO_2 dilution. It is worth noting that the CO_2 dilution adopted in this experimental study is not actually consistent with any EGR level. The relative N_2 content in EGR is expected to be higher than that in a pure CO_2 dilution.

The experimental apparatus consists of an ICCD camera for detecting CH* chemiluminescence and a gas analyzer for investigating the composition of the exhaust gases.

The details of the two high-temperature test points selected for the numerical models' validation are reported in Table 3.

3.2 Numerical setup and computational domain

Reactive high-fidelity simulations have been carried out using the fully compressible AVBP code (CERFACS, 2023). The third order in time and space TTGC numerical scheme (Colin and Rudgyard, 2000) has been used to discretize the convective term of the Navier–Stokes equations. The time discretization is explicit, and the timestep is automatically chosen in order to ensure a constant maximum CFL = 0.7. The dynamic Smagorinsky–Lilly formulation (Lilly, 1992) is used to treat the sub-grid fluctuations.

The turbulence chemistry interaction has been modeled using ATFM (Colin et al., 2000) with a constant thickening factor selected to ensure a constant number of grid points in the unstretched laminar flame front equal to 5.

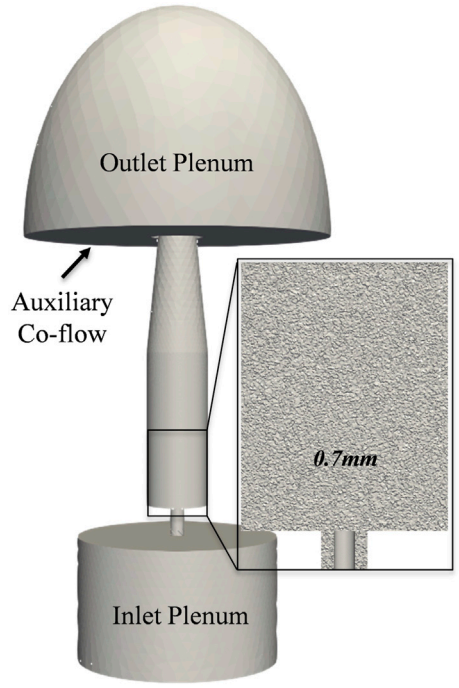

FIGURE 6
Computational domain and mesh detail in the flame stabilization region.

The computational domain is shown in Figure 6. At the inlet plenum, the mass flow condition is specified, whereas in the outlet plenum, the atmospheric pressure is prescribed on the dome and an auxiliary co-flow inlet has been assigned to the plenum ring. All the inlet and outlet boundaries are modeled with partially non-reflecting Navier–Stokes characteristic boundary conditions (NSCBCs) (Poinsot and Lelef, 1992). All the walls are modeled via the wall function approach. A fixed temperature has been imposed on the wall boundaries in the combustion chamber, and the estimated temperatures for the quartz, backplate, and the center body are 1000, 900, and 900 K, respectively. In terms of inlet temperature, mixture composition, and mass flow, the numerical boundary conditions are the same as described in Table 3 for the experimental test point.

3.3 Numerical results

The results discussion is organized as follows: first, the assessment of the flame prediction is focused with respect to the experimental measurements. Afterward, the impact of the heat loss on the flame shape is discussed, and finally a brief characterization of the numerically predicted flame dynamics is provided.

3.3.1 Flame prediction assessment

In Figure 7, the line of sight (LOS) of the time-averaged heat release rate (HR) is compared to the experimental CH* chemiluminescence for the two investigated cases. The numerical prediction of the flame for the case without CO_2 addition shows an M-shaped flame, which is stabilized near the swirler exit. However, only a weak trace of HR can be identified near the center body of the swirler and the backplate,

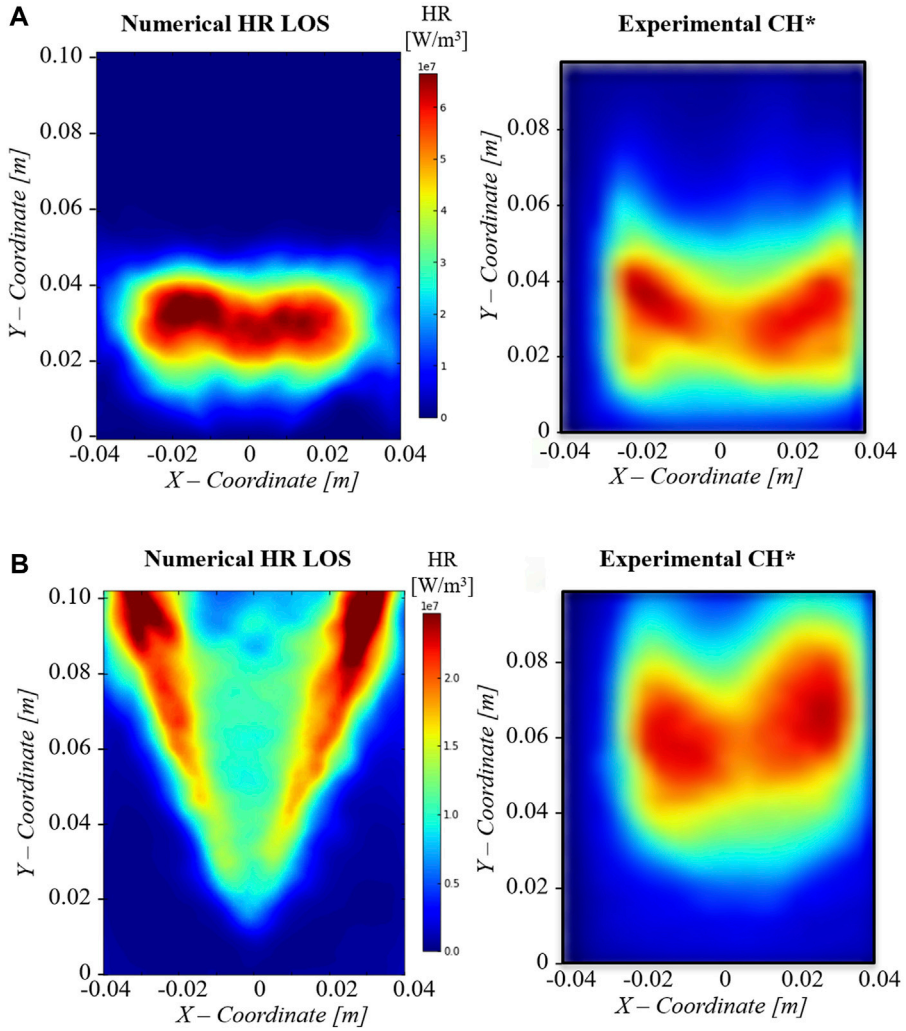

FIGURE 7
Comparison between the numerical time-averaged heat release rate (left) and the experimental CH* chemiluminescence (right) for the **(A)** CH_4–air case and **(B)** CH_4/CO_2/air case. All the maps are line-of-sight integrated.

where the wall heat loss plays a key role in the inhibition of flame stabilization, which will be pointed out later. Upon increasing the CO_2 content, the predicted flame topology changes, and the anchoring on the external shear layer gets completely lost. Moreover, in this CO_2-enriched case, a certain axial shift of the HR peak can be observed, indicating that the flame is globally approaching the blow-off due to the increase in both the CO_2 content and the mass flow. From this perspective, the simulations have been found capable of predicting the global change in the flame shape as well as the change in the stabilization mechanism observed experimentally, which is the main objective of this model validation experiment. Some discrepancies exist between the experimental and prediction results; there exist differences between the experimental CH* and the numerical heat-released map. An explanation for these discrepancies is that different quantities are considered for the comparison of the numerical and experimental data. The CH* is not necessarily fully representative of the heat release rate. In particular, for a very thick flame front and nearly distributed reaction zone (CO_2 diluted case), the comparison would not be so straightforward. The thick flame front would amplify the differences in the production region of the CH* with respect to the heat released, resulting in a mismatch between the two fields. Lauer et al. (2011) developed a procedure to correct the CH* and OH* chemiluminescence fields to retrieve the heat-released field. From the experimental data that are considered in this study, there is no possibility to perform such correction on the CH* field due to the lack of information about the flow field. A second possible reason for the observed difference is that when CO_2 is added, the flame approaches the blowout and its luminosity is expected to decrease significantly with the increasing noise. Eventually, the experimental investigation was not conducted aiming at validating numerical models, so there is a lack of data, such as the thermal boundary conditions and the flow field. On the other hand, this test case is the only study in the literature that characterizes an open geometry with optical measurements.

From the numerical side, the uncertainty of the wall thermal boundary partially precludes the accuracy of the solution in some regions. To highlight the role of the heat loss, the following section is dedicated to the investigation of the enthalpy defect effect on the local flame reactivity.

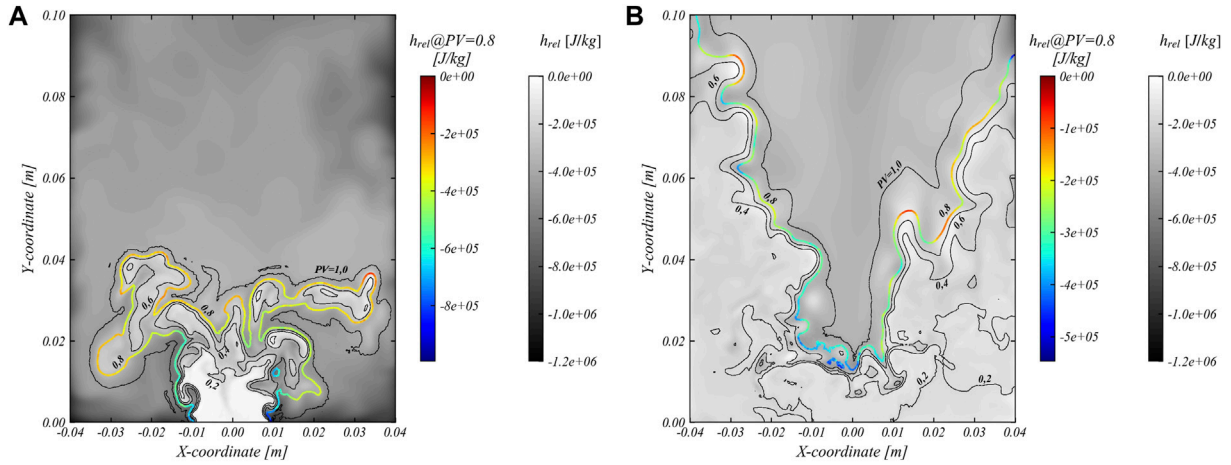

FIGURE 8
Instantaneous relative enthalpy contour. The isolines represent the progress variable computed according to Equation 7, with the PV = 0.8 isoline colored with the local relative enthalpy. **(A)** CH_4–air case; **(B)** CH_4/CO_2/air case.

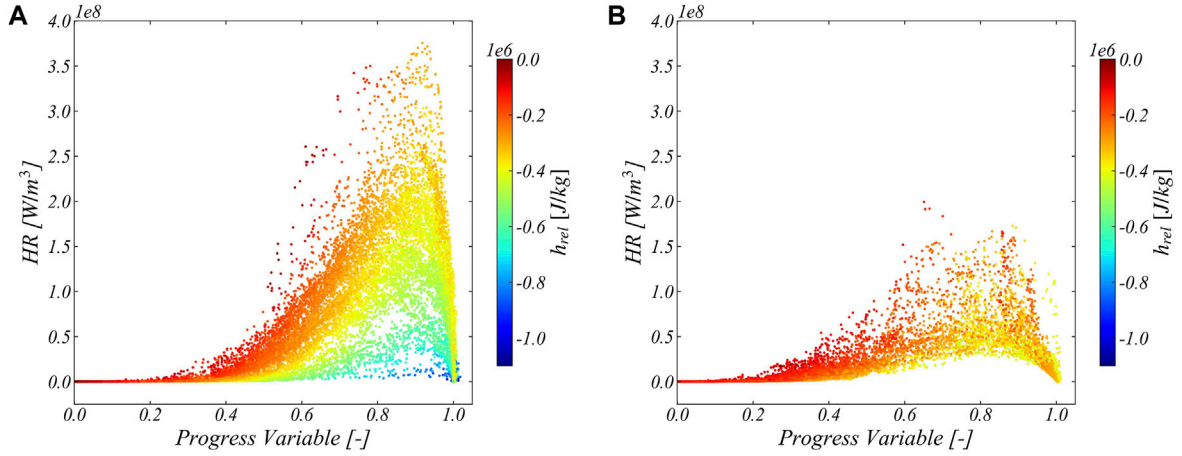

FIGURE 9
Instantaneous heat release rate dependence on the local progress variable on the chamber midplane colored by the level of relative enthalpy. **(A)** CH_4–air case; **(B)** CH_4/CO_2/air case.

3.3.2 Impact of heat loss on the flame

To investigate the role of wall heat loss (HL) in affecting the combustion process, the enthalpy h of the mixture has been computed as the sum of the sensible enthalpy h_s and the standard formation enthalpy h^0:

$$h = h_s + \sum_{k=1}^{N} Y_k \Delta h^0_{f,k}. \tag{5}$$

Here, N is the number of species in the mixture and $\Delta h^0_{f,k}$ is the standard formation enthalpy of the species k. The enthalpy defined in Eq. 5 is preserved under any adiabatic process; thus, any variation in this quantity during the combustion can be ascribed to the effect of the wall HL (neglecting the second-order contributions of the preferential diffusion). To define a parameter that can represent the local level of HL of the mixture with respect to the inlet fresh mixture enthalpy (h_u), the relative enthalpy has been defined as

$$h_{rel} = h - h_u. \tag{6}$$

Figure 8 shows the h_{rel} contour for the two investigated cases, and the h_{rel} is zero at the combustion chamber inlet fresh mixture and then decreases progressively due to the presence of the non-adiabatic walls. In the figure, some progress variable (PV) isolines have been reported. The progress variable has been defined as the sum of the CO and CO_2 species mass fraction $Y_{PV} = Y_{CO} + Y_{CO2}$ and then normalized as

$$PV = \frac{Y_{PV} - Y_{PV_u}}{Y_{PV_b} - Y_{PV_u}}. \tag{7}$$

Here, Y_{PV_b} and Y_{PV_u} are the unnormalized PVs evaluated for the burnt and the fresh mixture, respectively. The PV isolines allow highlighting the significant differences in the instantaneous flame topology of the two cases. The flame shape strongly affects the role

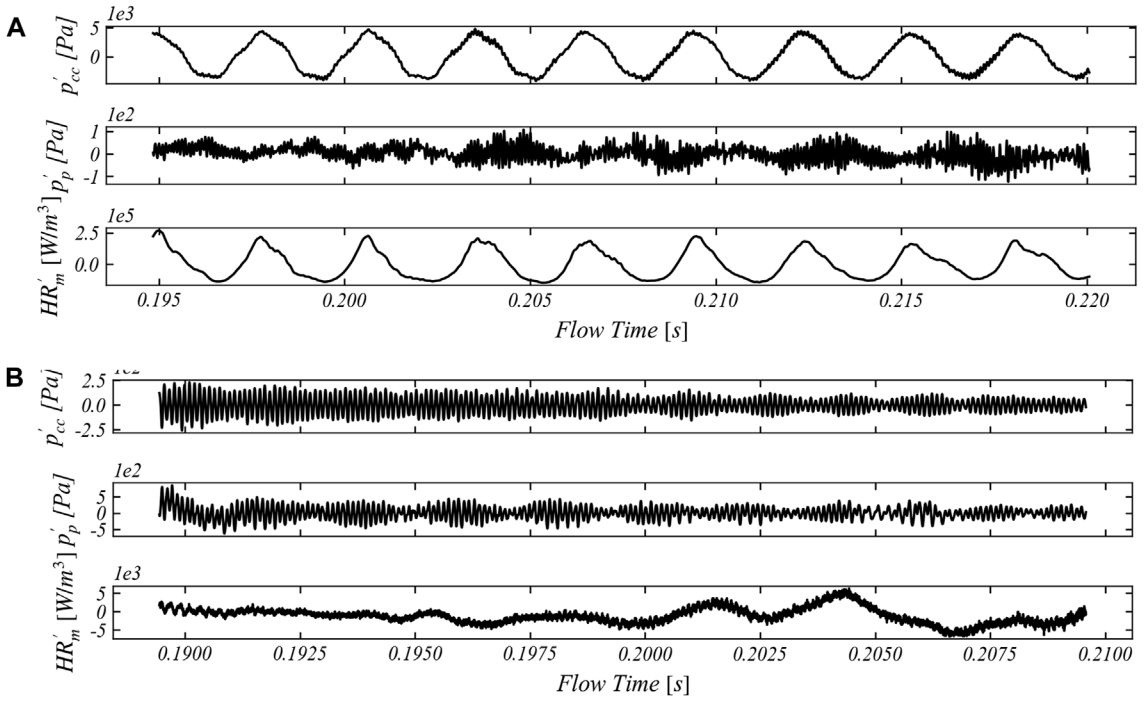

FIGURE 10
Predicted fluctuations of pressure in the combustion chamber p'_{cc}(probe on the axis y = 20 mm), pressure in the inlet plenum p'_p (probe on the axis y = −40 mm), and mean integral heat release rate HR'_m. **(A)** CH_4–air case; **(B)** CH_4/CO_2/air case.

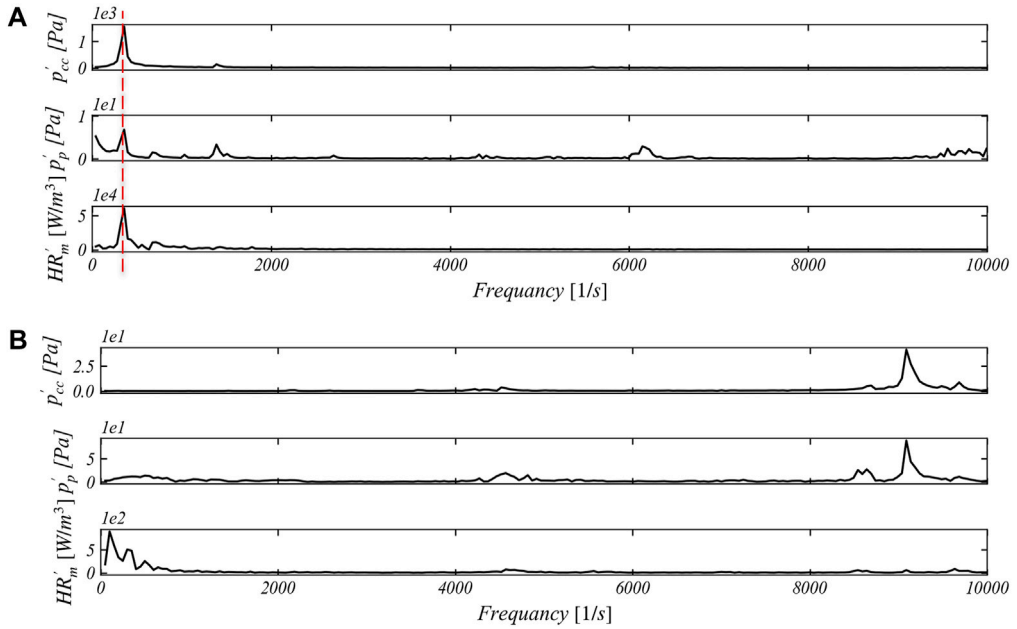

FIGURE 11
FFT of the signal of pressure in the combustion chamber p'_{cc}(probe on the axis y = 20 mm), pressure in the inlet plenum p'_p (probe on the axis y = −40 mm), and mean integral heat released rate HR'_m. **(A)** CH_4–air case; **(B)** CH_4/CO_2/air case.

of the wall heat losses in the CH_4–air case, stabilized on the external shear layer, and enhances the heat loss in the corner recirculation region (CRR) due to the high temperature of the recirculating combustion products. The enthalpy losses of this region affect the flame in the regions behind the backplate, as shown by the PV = 0.8 isoline colored with the local h_{rel}. The

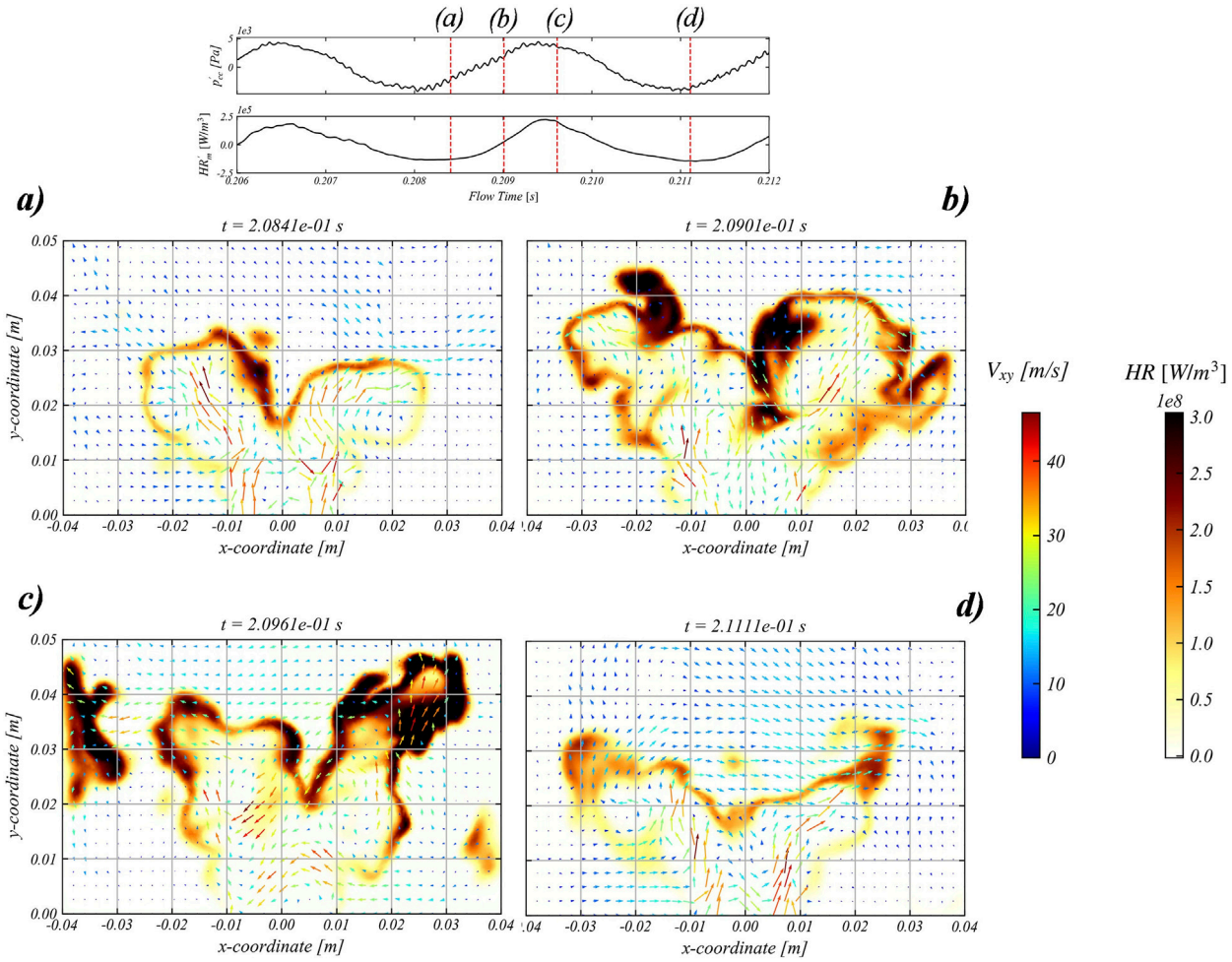

FIGURE 12
Instantaneous snapshots of the heat release rate and velocity vector on the midplane during a cycle of the flame dynamics for the CH_4–air case. **(A)** Low CC pressure, high fresh mixture inlet velocity, low HR; **(B)** Pressure and HR increase with inlet velocity decrease; **(C)** Highest HR and pressure with lowest fresh mixture inlet velocity; **(D)** Lowest pressure and HR with Highest fresh mixture inlet velocity.

colored isoline in Figure 8A shows that the higher losses are identified on the external shear layer, closer to the backplate, where the mixture reactivity and the fuel consumption are expected to be significantly slowed down by the enthalpy loss. On the contrary, the predicted V-shaped flame in the CO_2-enriched case allowed the CRR to be filled with low-temperature fresh gases limiting the HL in this region, as shown in Figure 8. Because of that, and the lower adiabatic flame temperature of the latter case, the flame is less affected by the HL.

Defining the flame stretch as the sum of the strain and curvature contribution (Poinsot and Veynante, 2005), the role of the flame front curvature on the local HL can be identified on the PV = 0.8 isoline (Figure 8B); the negative flame curvature regions are characterized by higher h_{rel} values, whereas the positive flame curvature regions are affected by much higher HL levels.

Investigating the stability characteristics of the flame is particularly interesting due to the effect of HL on the flame speed and, analogously, on the related HR. For this purpose, in Figure 9 the scatterplot of HR and PV has been reported with respect to the local h_{rel} level. The plots clearly show the decrease in HR, where h_{rel} is lower, highlighting the role of the local flame HL in slowing down the flame kinetics and, consequently, reducing the amount of heat released by the formation of the products. Comparing the two cases in Figure 9, it is evident that the CO_2-enriched case shows significantly lower HR values of approximately PV = 0.8 for the same level of h_{rel}. It is verified that the flame consumption speed is lower, despite the level of HL that affects this flame being less intensive. Moreover, it is worth noting that the higher HL level attributed to the burnt gases does not directly affect the combustion process. This is confirmed by the scatterplot in Figure 9, which shows that the lower h_{rel} values are clustered on PV = 1, where HR = 0.

3.3.3 Flame dynamics

The increase in the CO_2 content of the fresh gas mixture has been found to significantly cause changes in the flame dynamics in the simulations. In Figure 10, the pressure oscillations in the plenum and combustion chamber (CC) have been reported together with the mean instantaneous HR of the two cases. In the CH_4–air case

(Figure 10A), high-amplitude-pressure oscillations of the order of 5 kPa have been observed in CC, whereas the pressure oscillations appear strongly dumped in the inlet plenum, where the fluctuations are 100 Pa. Similar high-amplitude and low-frequency fluctuations are also observed in the mean HR signal for the CH_4–air case. With the addition of CO_2 in the mixture (Figure 10B), the pressure oscillations in the combustion chamber decrease in terms of amplitude and are comparable to the oscillations observed in the inlet plenum (200–500 Pa). In Figure 11, the similar signals in the frequency domain have been reported, and the aligned peaks in all the signals at the frequency of 356 Hz (Figure 11A) suggest the presence of a certain thermoacoustic coupling between the heat release rate and pressure fluctuations. On the contrary, for the CO_2-enriched case (Figure 11B), the pressure fluctuations appear decoupled from HR, and the two high-frequency peaks observed (Figure 11B) are completely out of the frequency range that could trigger any thermoacoustic coupling.

A visualization of the periodic flame dynamics for the CH_4–air case is shown in Figure 12. In the first snapshot (Figure 12A), the combustion chamber's instantaneous pressure is near its minimum, and the flame is very compact near the swirler exit, resulting in a global low heat release rate. The temporary lower pressure of the chamber with respect to the plenum enhances the fresh mixture entering the combustion chamber with a higher velocity. This is confirmed by the vector plot superimposed on the HR contour, which shows the high-velocity region near the CC inlet. The rapid fresh mixture refill enhances the increase in HR in the next phase, which in turn makes the pressure increase consistent, decreasing the pressure drop across the swirler feeding channel. The consequent slowdown of the inlet fresh mixture enhances the rapid fuel consumption (Figure 12C) until the flame once again becomes more compact (with lower HR), allowing the pressure to decrease again (Figure 12D).

These differences in the thermoacoustic responses observed in the two investigated cases can be due to the change in the flame shape, which in turn affects the temperature field and, thus, the speed of sound. In general, as mentioned previously, the increase in the CO_2 content of the mixture decreases the power density, and this has been found to be a beneficial effect in the mitigation of thermoacoustic coupling (ElKady et al., 2008; Evulet et al., 2009).

4 Conclusion

The impact of CO_2 addition on a swirled stabilized CH_4–air flame was numerically investigated. First, an automatic procedure for global reaction mechanism optimization has been presented and subsequently used to retrieve an optimized version of the BFER* two-step kinetics scheme for the CO_2-enriched environment. The optimization has been carried out considering several parameters in order to improve the prediction of different flame configurations, thermodynamic conditions, and mixture compositions. The novel BFER_CO_2* kinetics scheme shows that the level of accordance with the reference reaction mechanism is better for the freely propagating flames, whereas its response to the strain level of the premixed counterflow configuration could still be improved.

The BFER* and BFER_CO_2* mechanisms have been used to perform high-fidelity CFD simulations trying to numerically reproduce two flames experimentally investigated by De Persis et al. (2013): first without CO_2 dilution and second with 8.9% CO_2 (by volume in the oxidized state). The numerical prediction has been found capable of qualitatively reproducing the change in the flame topology, which moves from a lifted M-shaped flame in the CH_4–air case to a V-shaped flame with CO_2 addition. The effect of HL has been found to be the discriminating factor which, through the reactivity slowing down near the backplate, induces the flame lift-off in the CH_4–air case. With the CO_2 addition and the change in the flame shape, the effect of HL on the reactivity is mitigated. The lower HR rates prove the essential role of CO_2 in decreasing the speed capacity of the local flame consumption. This would have contributed to the change in flame shape and the stabilization mechanism observed in the two cases. Numerically, CO_2 dilution leads to a strong mitigation of the pressure oscillations that are observed in the methane–air case. Overall, the model has shown a satisfactory level of agreement with the experimental data, paving the way for the setup application for the study of real EGR cases.

Data availability statement

The raw data supporting the conclusion of this article will be made available by the authors, without undue reservation.

Author contributions

SC: Python script writing, numerical simulation running, and post-processing results. PN and AA: revision and support. All authors contributed to the article and approved the submitted version.

Acknowledgments

The authors would like to thank Professor G. Cabot for sharing the experimental data and CERFACS for the grant to use the AVBP code and the customized Cantera build.

Conflict of interest

The authors declare that the research was conducted in the absence of any commercial or financial relationships that could be construed as a potential conflict of interest.

Publisher's note

References

Adapted version of Cantera form CERFACS (2017). Adapted version of Cantera form CERFACS. Available at: https://www.cerfacs.fr/cantera/.

Burdet, A., Lachaux, T., De La Cruz García, M., and Winkler, D. (2010). "Combustion under flue gas recirculation conditions in a gas turbine lean premix burner," in *Proc. ASME Turbo Expo, Power for Land*, 1083–1091. doi:10.1115/GT2010-23396

Burnes, D., Saxena, P., and Dunn, P. (2020). Study of using exhaust gas recirculation on a gas turbine for carbon capture. *Proc. ASME Turbo Expo*. doi:10.1115/GT2020-16080

Cailler, M., Darabiha, N., and Fiorina, B. (2020). Development of a virtual optimized chemistry method. Application to hydrocarbon/air combustion. *Combust. Flame* 211, 281–302. doi:10.1016/j.combustflame.2019.09.013

CERFACS (2023). THIS IS the website of the AVBP code of CERFACS AVBP. Available at: https://www.cerfacs.fr/avbp7x/.

Chan, Y. L., Zhu, M., Zhang, Z., Liu, P., and Zhang, D. (2015). The effect of CO2 dilution on the laminar burning velocity of premixed methane/air flames. *Energy Procedia* 75, 3048–3053. Elsevier B.V. doi:10.1016/j.egypro.2015.07.621

Chen, Y., Wang, J., and Zhang, X. (2020). Experimental and numerical study of the effect of CO2 replacing part of N2 present in air on CH4 premixed flame characteristics using a reduced mechanism. *ACS Omega* 5 (46), 30130–30138. doi:10.1021/acsomega.0c04537

Cohé, C., Chauveau, C., Gökalp, I., and Kurtuluş, D. F. (2009). CO2 addition and pressure effects on laminar and turbulent lean premixed CH4 air flames. *Proc. Combust. Inst.* 32, 1803–1810. II. doi:10.1016/j.proci.2008.06.181

Colin, O., Ducros, F., Veynante, D., and Poinsot, T. (2000). A thickened flame model for large eddy simulations of turbulent premixed combustion. *Phys. Fluids* 12 (7), 1843–1863. doi:10.1063/1.870436

Colin, O., and Rudgyard, M. (2000). Development of high-order taylor-galerkin schemes for LES. *J. Comput. Phys.* 162 (2), 338–371. doi:10.1006/jcph.2000.6538

De Persis, S., Cabot, G., Pillier, L., Gökalp, I., and Boukhalfa, A. M. (2013). Study of lean premixed methane combustion with CO2 dilution under gas turbine conditions. *Energy Fuels* 27 (2), 1093–1103. doi:10.1021/ef3016365

Duva, B. C., Chance, L. E., and Toulson, E. (2020). Dilution effect of different combustion residuals on laminar burning velocities and burned gas Markstein lengths of premixed methane/air mixtures at elevated temperature. *Fuel* 267 (1), 117153. Elsevier. doi:10.1016/j.fuel.2020.117153

ElKady, A. M., Evulet, A., Brand, A., Ursin, T. P., and Lynghjem, A. (2008). "Exhaust gas recirculation in dln f-class gas turbines for post-combustion C02 capture," in *Proc. ASME Turbo Expo*, 847–854. doi:10.1115/GT2008-51152

Erete, J. I., Hughes, K. J., Ma, L., Fairweather, M., Pourkashanian, M., and Williams, A. (2017). Effect of CO2 dilution on the structure and emissions from turbulent, non-premixed methane–air jet flames. *J. Energy Inst.* 90 (2), 191–200. Elsevier Ltd. doi:10.1016/j.joei.2016.02.004

Evulet, A. T., Elkady, A. M., Branda, A. R., and Chinn, D. (2009). On the performance and operability of GE's dry low NO combustors utilizing exhaust gas recirculation for PostCombustion carbon capture. *Energy Procedia* 1, 3809–3816. doi:10.1016/j.egypro.2009.02.182

Franzelli, B. G. (2011). *Impact of the chemical description on direct numerical simulations and large eddy simulations of turbulent combustion in industrial aero-engines*, 270. PhD.

Galmiche, B., Halter, F., Foucher, F., and Dagaut, P. (2011). Effects of diluents addition on laminar burning velocity of premixed methane/air flames. *Energy and Fuels* 39, 1557–1562. doi:10.3969/j.issn.0253-374x.2011.10.027

Guethe, F., Stankovic, D., Genin, F., Syed, K., and Winkler, D. (2011). "Flue gas recirculation of the Alstom sequential gas turbine combustor tested at high pressure," in *Proc. ASME Turbo Expo*, 399–408. doi:10.1115/GT2011-45379

Halter, F., Foucher, F., Landry, L., and Mounaïm-Rousselle, C. (2009). Effect of dilution by nitrogen and/or carbon dioxide on methane and iso-octane air flames. *Combust. Sci. Technol.* 181 (6), 813–827. doi:10.1080/00102200902864662

Han, D., Satija, A., Gore, J. P., and Lucht, R. P. (2018). Experimental study of CO2 diluted, piloted, turbulent CH4/air premixed flames using high-repetition-rate OH PLIF. *Combust. Flame* 193, 145–156. Elsevier Inc. doi:10.1016/j.combustflame.2018.03.012

Han, D., Satija, A., Kim, J., Weng, Y., Gore, J. P., and Lucht, R. P. (2017). Dual-pump vibrational CARS measurements of temperature and species concentrations in turbulent premixed flames with CO2 addition. *Combust. Flame* 181, 239–250. Elsevier Inc. doi:10.1016/j.combustflame.2017.03.027

Hejie, L., Ahmed, E., and Andrei, E. (2009). "Effect of exhaust gas recirculation on NOx formation in premixed combustion system," in 47th AIAA Aerospace Sciences Meeting including The New Horizons Forum and Aerospace Exposition, Orlando, Florida, 05 January 2009 - 08 January 2009, 1–12. doi:10.2514/6.2009-226

Jourdaine, P., Mirat, C., Caudal, J., Lo, A., and Schuller, T. (2017). A comparison between the stabilization of premixed swirling CO2-diluted methane oxy-flames and methane/air flames. *Fuel* 201, 156–164. Elsevier Ltd. doi:10.1016/j.fuel.2016.11.017

Kobayashi, H., Hagiwara, H., Kaneko, H., and Ogami, Y. (2007). Effects of CO2 dilution on turbulent premixed flames at high pressure and high temperature. *Proc. Combust. Inst.* 31 (1), 1451–1458. I. doi:10.1016/j.proci.2006.07.159

Lauer, M., Zellhuber, M., Sattelmayer, T., and Aul, C. J. (2011). Determination of the heat release distribution in turbulent flames by a model based correction of OH* chemiluminescence. *J. Eng. Gas Turbines Power* 133 (12), 1–9. doi:10.1115/1.4004124

Li, H., Ditaranto, M., and Berstad, D. (2011). Technologies for increasing CO2 concentration in exhaust gas from natural gas-fired power production with post-combustion, amine-based CO2 capture. *Energy* 36 (2), 1124–1133. Elsevier Ltd. doi:10.1016/j.energy.2010.11.037

Lilly, D. K. (1992). A proposed modification of the Germano subgrid-scale closure method. *Phys. Fluids* 4 (3), 633–635. doi:10.1063/1.858280

Nassini, P. C., Pampaloni, D., Meloni, R., and Andreini, A. (2021). Lean blow-out prediction in an industrial gas turbine combustor through a LES-based CFD analysis. *Combust. Flame* 229, 111391. Elsevier Inc. doi:10.1016/j.combustflame.2021.02.037

Poinsot, T. J., and Lelef, S. K. (1992). Boundary conditions for direct simulations of compressible viscous flows. *J. Comput. Phys.* 101 (1), 104–129. doi:10.1016/0021-9991(92)90046-2

Poinsot, T., and Veynante, D. (2005). *Theoretical and numerical combustion*. 2. Morningside, Australia: R.T. Edwards Commercial.

Smith, G. P., Golden, D. M., Frenklach, M., Moriarty, N. W., Eiteneer, B., Goldenberg, M., et al. (2000). gri3.0. Available at: http://combustion.berkeley.edu/gri-mech/.

Vandel, A., Chica Cano, J., de Persis, S., and Cabot, G. (2020). Study of the influence of water vapour and carbon dioxide dilution on flame structure of swirled methane/oxygen-enriched air flames. *Exp. Therm. Fluid Sci.* 113, 110010. Elsevier. doi:10.1016/j.expthermflusci.2019.110010

Xie, M., Fu, J., Zhang, Y., Shu, J., Ma, Y., Liu, J., et al. (2020). Numerical analysis on the effects of CO2 dilution on the laminar burning velocity of premixed methane/air flame with elevated initial temperature and pressure. *Fuel* 264, 116858. Elsevier. doi:10.1016/j.fuel.2019.116858

Nomenclature

Acronyms

ATFM	artificially thickened flame model	
CC	combustion chamber	
CCS	carbon capture and storage	
CF	cost function	
DLN	dry low NOx	
EGR	exhaust gas recirculation	
HR	heat release rate	[W/m^3]
lhs	Latin hypercube sampling	
LOS	line of sight	
PQ	predicted quantity	
PV	progress variable	[-]
TQ	target quantity	

Symbols

A_k	Arrhenius pre-exponential factor	
b_k	Arrhenius temperature exponent	[-]
D_t	thermal flame thickness	[m]
Ea_k	Arrhenius activation energy	
h	chemical and sensible enthalpy	[J/kg]
n_k	reaction order	
N	generic dimension	
p	static pressure	[Pa]
S_c	Schmidt number	[-]
S_{fuel}	fuel consumption speed	[m/s]
T	static temperature	[K]

Greek symbols

Φ	equivalence ratio	[-]
μ	laminar viscosity	
ρ	density	[kg/m^3]

Subscripts

b	burnt
f	formation
m	mean
p	plenum
ref	reference
rel	relative